








Low-energy cross-section measurement of the $^{10}\text{B}(\alpha, n)^{13}\text{N}$ reaction and its impact on neutron production in first-generation stars

Q. Liu,¹ M. Febraro,² R. J. deBoer,¹ S. Aguilar,¹ A. Boeltzig ^{1,*} Y. Chen ¹ M. Couder ¹ J. Görres,¹ E. Lamere,^{1,†} S. Lyons,^{1,‡} K. T. Macon,^{1,3} K. Manukyan ¹ L. Morales ¹ S. Pain,² W. A. Peters,² C. Seymour,¹ G. Seymour ^{1,§} R. Toomey,⁴ B. Vande Kolk,¹ J. Weaver,⁵ and M. Wiescher ¹

¹The Joint Institute for Nuclear Astrophysics, Department of Physics, Notre Dame, Indiana 46556, USA

²Oak Ridge National Laboratory, Oak Ridge, Tennessee 37830, USA

³Department of Physics and Astronomy, Louisiana State University, Baton Rouge, Louisiana 70803, USA

⁴Department of Physics and Astronomy, Rutgers University, Piscataway, New Jersey 08854, USA

⁵Materials Measurement Laboratory, National Institute of Standards and Technology, Gaithersburg, Maryland 20899, USA



(Received 7 November 2019; accepted 27 January 2020; published 26 February 2020)

Nucleosynthesis in the first generation of massive stars offers a unique setting to explore the creation of the first heavier nuclei in an environment free of impurities from earlier stellar generations. In later generations of massive stars, hydrogen burning occurs predominantly through the CNO cycles, but without the carbon, nitrogen, and oxygen to catalyze the reaction sequence, first stars would have to rely on the inefficient pp chains for their energy production. Observations of second and third generation stars show pronounced abundances of carbon and oxygen isotopes, which suggests a rapid conversion of the primordial abundances to heavier elements. While the triple-alpha-process primarily facilitates this conversion, there are alternative reaction sequences, such as $^2\text{H}(\alpha, \gamma)^6\text{Li}(\alpha, \gamma)^{10}\text{B}(\alpha, n)^{13}\text{N}$, that may play a significant role. To study such alternate reaction pathways for production of carbon and heavier nuclei, a number of new measurements are needed. In this work, new measurements are reported for the $^{10}\text{B}(\alpha, n)^{13}\text{N}$ reaction, extending the cross section down to 575 keV incident α -particle energy. The measurements were made using a state-of-the-art deuterated liquid scintillator and a spectrum unfolding technique. An R -matrix analysis was performed in order to facilitate a comparison of the underlying nuclear structure with the reaction measurements. An unexpected upturn is observed in the low-energy S factor that indicates the presence of a new low-energy resonance. A revised reaction rate is determined that takes into account the present data as well as other previous measurements from the literature that were previously neglected.

DOI: [10.1103/PhysRevC.101.025808](https://doi.org/10.1103/PhysRevC.101.025808)

I. INTRODUCTION

The nucleosynthesis in first generation stars is primarily fueled by reactions on the H and He abundances produced in the big bang. The energy generation in massive primordial stars is therefore characterized by a nucleosynthesis reaction pattern that is completely different from the ones powering present generation massive stars. The lack of carbon and oxygen in primordial material means that hydrogen burning is constrained to the pp chains without any CNO cycle contributions [1]. Since the energy production through the pp chains is limited by the slow, weak-interaction-based fusion of two protons to deuterium [2], the internal energy release

cannot compensate for the gravitational contraction of the massive star. This causes a gradual increase in temperature and density until helium burning ignites through the 3α process [3], producing the first generation of ^{12}C and subsequently ^{16}O through the $^{12}\text{C}(\alpha, \gamma)^{16}\text{O}$ radiative capture reaction [4]. Both ^{12}C and ^{16}O are observable in pronounced abundances in the oldest—second or third—generation stars in our universe [5,6].

The 3α process presumably serves as the main reaction link between primordial ^4He and ^{12}C and ^{16}O abundances. However, previous analyses identified alternative deuterium-driven reaction patterns feeding CNO elements that may occur at certain temperature and density conditions in primordial stellar environments [7]. Yet, these reaction links were handicapped by insufficient amounts of primordial deuterium for these alternative reaction sequences to emerge. This paper discusses two further reaction sequences linking ^4He with the CNO mass range; these are the reaction branches $^2\text{H}(\alpha, \gamma)^6\text{Li}(\alpha, \gamma)^{10}\text{B}(\alpha, n)^{13}\text{N}$ and alternatively $^2\text{H}(\alpha, \gamma)^6\text{Li}(\alpha, \gamma)^{10}\text{B}(\alpha, d)^{12}\text{C}$. The first α capture on ^{10}B may generate an appreciable neutron flux in the first star environment and the second reaction channel will provide new deuterium fuel generating a fuel cycle that bridges both

*Present address: Gran Sasso National Laboratory (LNGS), Via G. Acitelli 22, 67100 Assergi (AQ), Italy.

†Present address: Environment, Health & Safety Office, Massachusetts Institute of Technology Cambridge, Massachusetts, 02139, USA.

‡Present address: National Superconducting Cyclotron Laboratory, Michigan State University, East Lansing, Michigan 48824, USA.

§Present address: Rutgers University, Piscataway, New Jersey 08854, USA.

the mass 5 and 8 gaps. It should be noted that this cycle has strong leakage due to competing hydrogen-induced reactions such as ${}^6\text{Li}(p, \alpha){}^3\text{H}$ and ${}^{10}\text{B}(p, \alpha){}^7\text{Be}$, but to determine the efficiency of this reaction path more experimental information on the α -induced reactions on ${}^6\text{Li}$ and ${}^{10}\text{B}$ is necessary, as outlined below.

A comprehensive study has been made of low-energy ($1.0 < E_\alpha < 2.0$ MeV) ${}^{10}\text{B} + \alpha$ reactions previously by Shire *et al.* [8] and Shire and Edge [9]; however, their experimental data are not available in a detailed form. Manning and Singh [10] measured the ${}^{10}\text{B}(\alpha, p_0){}^{13}\text{C}$ reaction even slightly lower in energy ($E_\alpha \approx 0.95$ MeV), reporting an additional weak resonance. Gallmann *et al.* [11] and Stanley [12] made measurements of secondary γ rays from the ${}^{10}\text{B}(\alpha, p\gamma){}^{13}\text{C}$ reaction down to $E_\alpha = 1.0$ MeV. Additionally, measurements have been made down to $E_\alpha = 1.4$ MeV by Van der Zwan and Geiger [13] for the ${}^{10}\text{B}(\alpha, n){}^{13}\text{N}$ reaction at $\theta_{\text{lab}} = 0^\circ$ and 90° , Chen *et al.* [14] for the ${}^{10}\text{B}(\alpha, p_0){}^{13}\text{C}$ reaction at $\theta_{\text{lab}} = 90^\circ$, and Talbott and Heydenburg [15] for the ${}^{10}\text{B}(\alpha, p\gamma){}^{13}\text{C}$ reaction at $\theta_{\text{lab}} = 90^\circ$. McIntyre *et al.* [16] have also made lowenergy measurements of the ${}^{10}\text{B}(\alpha, \alpha_0){}^{10}\text{B}$ reaction down to $E_\alpha = 1.0$ MeV. This limited amount of data is all that is available for lowenergy ${}^{10}\text{B} + \alpha$ reactions. Several additional measurements have been performed that cover a similar excitation energy range in the ${}^{14}\text{N}$ compound system, for the ${}^{13}\text{C} + p$ [17,18] and ${}^{12}\text{C} + d$ [19–45] reactions, but the comparison of resonances properties is complicated by the population of several additional resonances in these reactions as well as a strong direct component of the cross section.

To explore the impact of the ${}^{10}\text{B}(\alpha, n){}^{13}\text{N}$ reaction on the primordial reaction chains and the associated release of neutrons in an early star environment, we have performed experiments studying the strength of α -induced reactions on ${}^{10}\text{B}$ at very low energies at the Nuclear Science Laboratory (NSL) of the University of Notre Dame. The low-energy measurements presented here have been followed up by the higher-energy measurement of Liu *et al.* [46]. In Sec. II, the setup and measurement of the ${}^{10}\text{B}(\alpha, n){}^{13}\text{N}$ reaction are described. The calculation of the cross sections from the observed yields is described in Sec. III. The R -matrix analysis of the resulting cross section, combined with complementary data from other α -induced reactions, is discussed in Sec. IV. Discussions of the interpretation of the new measurements on the underlying nuclear structure are given in Sec. V, and the reaction rate is calculated in Sec. VI. A summary is given in Sec. VII.

II. EXPERIMENTAL METHODS

The ${}^{10}\text{B}(\alpha, n){}^{13}\text{N}$ reaction [$Q = 1.05873(27)$ MeV] was studied in the range $570 < E_\alpha < 2500$ keV at the University of Notre Dame Nuclear Science Laboratory. The Sta. ANA pelletron accelerator was used to produce a beam of He^+ ions with an intensity of between 0.1 and 60 μA on target. At high energies, on strong resonances, the beam intensity was limited to prevent dead time in the data acquisition system (DAQ). The DAQ consisted of a CAEN V1751 1 GHz 10-bit digitizer. Data were transferred from the V1751 to a computer using a fiber optic link.

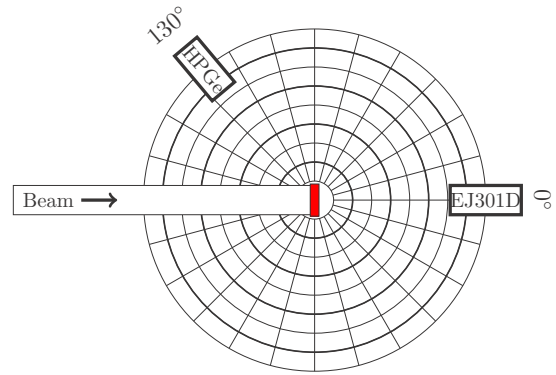


FIG. 1. Experimental Setup (not to scale). A deuterated liquid scintillator detector was placed at $\theta_{\text{lab}} = 0$ (EJ301D) at a distance of 20.9 cm from the target to measure prompt neutrons. An HPGe was placed at $\theta_{\text{lab}} = 130^\circ$ at a distance of 21.5 cm to detect secondary γ -rays. At low energies ($E_\alpha < 1.0$ MeV), the EJ301D at 0° was moved to 5.5 cm from the target.

The detector setup was made up of a deuterated liquid scintillator detector of type EJ301D [47] (size: 7.6 cm thick \times 5.8 cm diameter) and a high-purity germanium detector (HPGe) with a relative efficiency of 54%, as shown in Fig 1. Excitation curve and angular distribution measurements were made with the EJ301D detector, which is a newly developed xylene-based scintillator with improved pulse-shape discrimination (PSD). The detector was placed on a swing arm that was rotated to angular positions of 0° , 30° , 60° , 90° , 110° , 135° , and 155° with respect to the beam direction for the angular distribution measurements. An excitation function was measured at 0° in order to achieve the highest neutron energies at low beam energies.

At high energies, from 1.0 to 2.5 MeV, where the count rate was also high, the scintillators were placed in far geometry at a distance of 20.9 cm. As the beam energy went down below 1 MeV, the EJ301D detector at 0° was moved into a close geometry of 5.5 cm for higher efficiency. In addition, excitation curves were also measured for the ${}^{10}\text{B}(\alpha, p_{1,2,3}\gamma){}^{13}\text{C}$ reactions [$E_x = 3.089443(20)$, $3.684507(19)$, and $3.853807(19)$ MeV] using an HPGe detector at 130° . The distance between the target and HPGe detector face was 21.5 cm.

The target was prepared by electron-gun sputtering a thin layer of enriched [96.2(5)%] ${}^{10}\text{B}$ powder onto a 0.5 mm thick tantalum backing. The thickness and uniformity of the target were measured at the National Institute for Standards and Technology (NIST) Center for Neutron Research (NCNR) using cold neutron depth profiling with the neutron standard ${}^{10}\text{B}(n, \alpha){}^7\text{Li}$ reaction [48–52]. Six points of 3 mm diameter were measured across the beam spot area (10.4 mm diameter) of the target surface as well as a portion of the target that had not been exposed to beam. These measurements were used to determine both the initial thickness of the target and the amount of degradation that occurred over the experimental run. An initial thickness of $0.70(3)$ $\mu\text{g}/\text{cm}^2$ determined. The uncertainty is dominated by the homogeneity of the evaporation process for the target. Significant degradation of the target was observed, which was consistent with the observed

change in yield as a function of integrated beam on target. The corrections for the target degradation were made assuming a linear dependence with the integrated charge on target. The measurements were made by making repeated energy scans over overlapping energy ranges, providing a cross-check for the degradation rate. Over the course of the experiment a total degradation of 40% was observed. The target degradation had a significant affect on the uncertainty of the data. Repeated measurements at similar energies found that a 15% point-to-point uncertainty resulted from the target degradation. Further details of the NIST target characterization can be found in the Supplemental Material [53].

The maximum energy loss through the fresh target was 1.5 keV for an α -particle beam at $E_\alpha = 575$ keV. As the cross section is dominated by resonances with total widths much larger than this maximum energy loss, no target effect corrections were needed. As the uncertainty in the beam energy (± 2 keV) is comparable to this energy loss, no effective energy correction was made.

Contributions to the overall systematic uncertainty for the $^{10}\text{B}(\alpha, n)^{13}\text{N}$ data include target thickness (5%), beam charge integration (3%), and efficiency (10%) for a total systematic uncertainty of 12%. For the $^{10}\text{B}(\alpha, p\gamma)^{13}\text{C}$ data, the uncertainty in the γ -ray efficiency is 6%, giving a total systematic uncertainty for that data of 8%.

III. ANALYSIS

The energy calibration of the light response spectrum was carried out using a ^{137}Cs source, with the well-known single γ ray at $E_\gamma = 661.7$ keV. The deuteron and electron recoil peaks from incident neutrons and γ rays can be well separated using pulse shape discrimination down to an electron-equivalent energy threshold of 190 keVee, which corresponds to an incident neutron energy of approximately 1 MeV. A ^{252}Cf source was used to define the neutron gate; an example spectrum is shown in Fig. 2, where the vertical axis is the ratio of the tail pulse gate (180 ns) on the detector wave form to the total pulse gate (250 ns) (S/L). The neutron gate is bounded by the three red lines in Fig. 2, which represent the γ -ray upper bound, the neutron lower bound, and the neutron

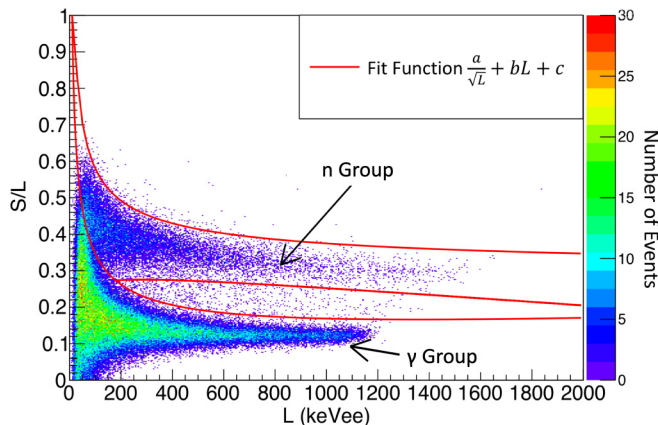


FIG. 2. Pulse shape discrimination: S/L as a function of L . The neutron gate is defined by the region inside three red lines.

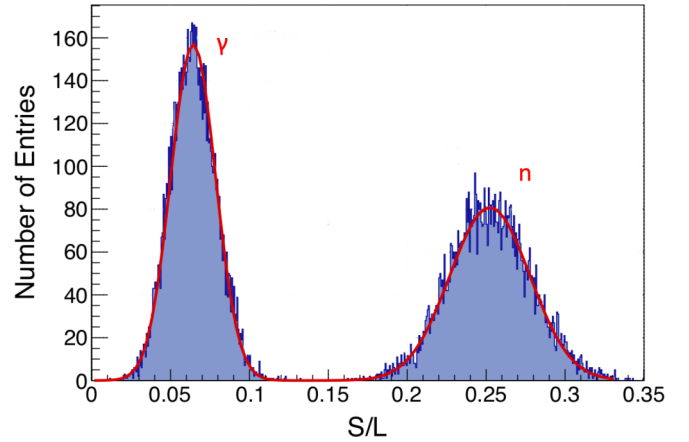


FIG. 3. Projection of Fig. 2 at $L = 350$ keVee.

upper bound. All have the functional form of $\frac{a}{\sqrt{L}} + bL + c$, in which the $\frac{a}{\sqrt{L}}$ term represents the statistical fluctuation of photons. Each bound line represents a 5σ deviation from the centroids of the γ /neutron peak in an S/L projection, as shown in Fig. 2. This is better illustrated by projecting a 1D spectrum of S/L for a fixed total pulse gate value L , as shown in Fig. 3.

A. Spectrum unfolding by the MLEM method

The light output spectra obtained from the detector is in fact a deuteron-recoil spectra, which result from the convolution of the incident neutron spectrum and the detector's response. Mathematically, this process can be expressed with a discrete linear matrix multiplication approximation [54],

$$y_i = \sum_{j=1}^J r_{ij} x_j, \quad i = 1, \dots, I, \quad (1)$$

where y_i is the number of counts falling in the i th bin of the light output spectra, x_j is the incident neutron flux with the same energy, and r_{ij} is an element of the response matrix R of the detector. Figure 4 shows how the response matrix maps the incident neutron flux space to the light output space. The process of extracting the incident neutron spectrum x is known as spectrum unfolding. The most straightforward approach to solving the unfolding problem is direct matrix inversion; however, it usually introduces larger noise in the final unfolded neutron spectrum than that of the data, since the response matrix R is highly ill-conditioned [55]. For this reason, various approximation approaches and codes have been developed to solve this problem. The method used in this work is known as maximum-likelihood expectation-maximization (MLEM). The MLEM method is equivalent to a maximum likelihood given that the binned number of counts in channel i of the pulse-height spectrum follows a Poisson distribution, which takes the form of

$$P_i = \frac{\lambda_i^{y_i} e^{-\lambda_i}}{y_i!}, \quad (2)$$

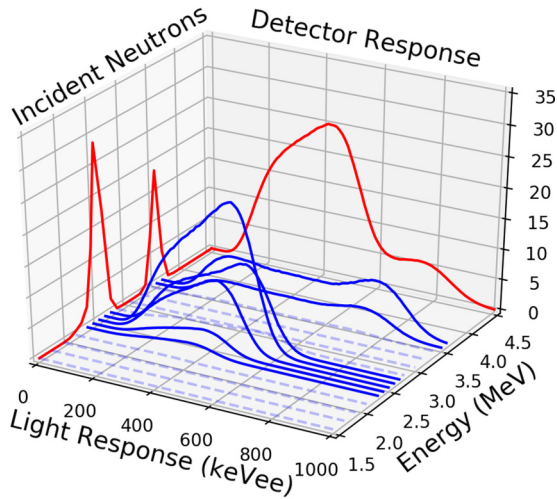


FIG. 4. Graphical interpretation of spectrum unfolding as given by Eq. (1).

where $\lambda_i = \sum_{j=1}^J r_{ij} x_j$ is the expected value of y_i . Then the log-likelihood function, which represents the probability of obtaining the measured light output, can be established. A detailed derivation by Pehlivanovic *et al.* [54] shows the final form of the MLEM algorithm takes the form

$$x_j^{(k+1)} = \frac{x_j^{(k)}}{\sum_{i=1}^I r_{ij}} \sum_{i=1}^I r_{ij} \frac{y_i}{\sum_{l=1}^J r_{il} x_l^{(k)}}, \quad j = 1, \dots, J, \quad (3)$$

where $x_j^{(k)}$ stands for the estimation of the j th neutron flux at the k th iteration. The iterative MLEM method given by Eq. (3) can also be derived from Bayes's theorem without the assumption of Poisson statistics or introducing a maximum likelihood [56].

The response matrix is modeled using MCNP-POLOMI [57,58] and tuned to match calibration measurements by way of phenomenological descriptions of the light response and resolution functions [59].

An unfolded spectrum from the $^{10}\text{B}(\alpha, n)^{13}\text{N}$ measurement at $\theta_{\text{lab}} = 0^\circ$ is shown in Fig. 5. Neutron deexcitations to the ground state are clearly observed for the $^{10}\text{B}(\alpha, n)^{13}\text{N}$ reaction. Also observed are beam-induced background reactions on ^{11}B and ^{13}C target impurities causing ground state transition such as the $^{11}\text{B}(\alpha, n)^{14}\text{N}$ and $^{13}\text{C}(\alpha, n)^{16}\text{O}$ reactions. The light output spectrum, shown by the red line in Fig. 5, was constructed and a threshold of $E_L = 190$ keVee (corresponding to about 1 MeV in neutron energy) was imposed based on the PSD limitations shown in Fig. 2. The incident neutron spectrum, as shown in the top panel of Fig. 5, was extracted using the MLEM algorithm. The blue line in the bottom panel of Fig. 5 represents the estimation of the light output spectrum by forward feeding the unfolded neutron spectrum through Eq. (1). It serves as a verification of the unfolding process.

In order to gauge the performance of the unfolding algorithm given the statistics of each spectrum, a Monte Carlo procedure is used. This is implemented by generating and unfolding numerous randomly generated pseudo light response

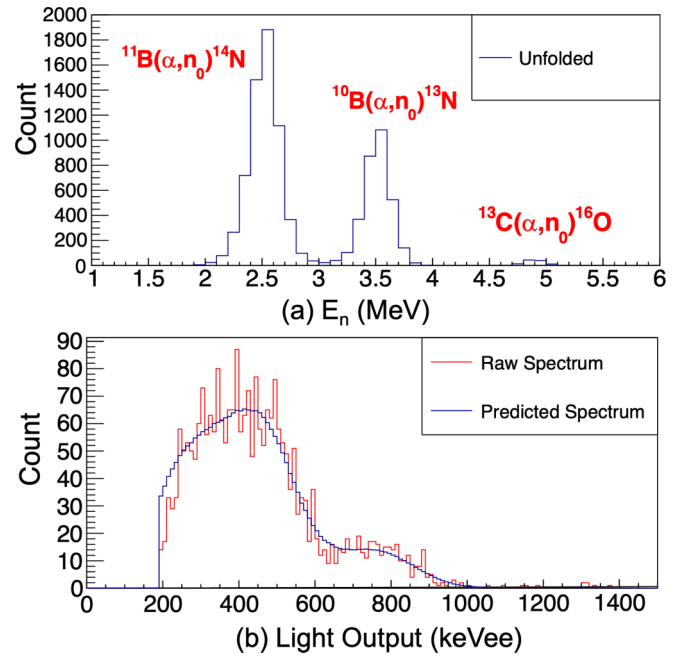


FIG. 5. The top panel (a) of the figure shows the unfolded neutron spectrum (blue histogram) from the ^{10}B target at $\theta_{\text{lab}} = 0^\circ$ and $E_\alpha = 2.5$ MeV. The bottom panel (b) shows the raw light response (red histogram) and the modeled light response (blue solid line). See text for details.

spectra based on the measured raw spectra. The procedure of uncertainty estimation using this method is as follows:

- (1) Create a Poisson distribution and take the bin content in the light response spectrum as the mean value.
- (2) Reconstruct a new spectrum by generating random counts for each bin in the light response spectrum with a Poisson random number generator.
- (3) Repeat the above steps for a large number of iterations, and extract the neutron counts distribution as a histogram.
- (4) Fit a Gaussian distribution to the histogram in (3), then take the standard deviation as the estimated uncertainty.

While this method gauges the reliability of the unfolding algorithm and estimates the uncertainty based on the statistics of the light response spectrum, the uncertainties in the response matrix itself have not yet been implemented.

B. Deuterated liquid scintillator detector efficiency

The neutron detector intrinsic efficiency was simulated using MCNPX-POLIMI, as shown in Fig. 6. Since the intrinsic efficiency of the deuterated liquid scintillators is threshold dependent, neutrons with energies lower than 1 MeV were cut off. The simulation is compared to the experimentally measured efficiency reported by Febbraro *et al.* [59], which was obtained using the $^{27}\text{Al}(d, n)^{28}\text{Si}$ reaction at $E_d = 7.44$ MeV and the $^9\text{Be}(d, n)^{10}\text{B}$ reaction at $E_d = 7.00$ MeV [60,61]

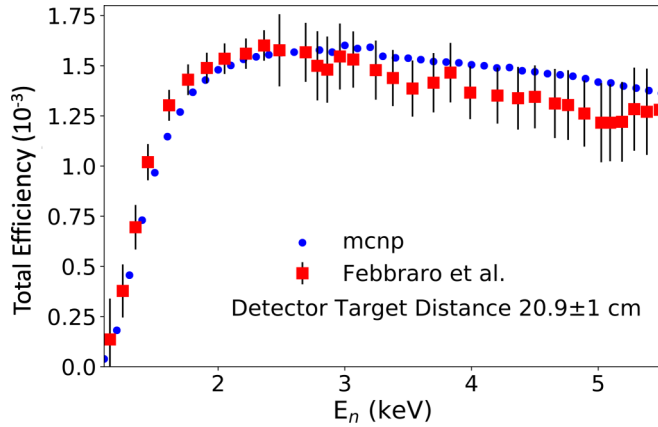


FIG. 6. Simulated intrinsic efficiency of a 3 in. \times 2 in. EJ301D detector with a threshold of 190 keVee.

at Ohio University. The efficiency is estimated to have an uncertainty of 10%.

C. γ -ray yields

As described in Sec. II, the deuterated liquid scintillators were paired with an HPGe detector to detect $^{10}\text{B} + \alpha$ reactions that produce secondary γ rays. Over the energy range of the present measurement these reactions are $^{10}\text{B}(\alpha, \alpha_1\gamma)^{10}\text{B}$, $^{10}\text{B}(\alpha, p_1\gamma)^{13}\text{C}$, $^{10}\text{B}(\alpha, p_2\gamma)^{13}\text{C}$,

and $^{10}\text{B}(\alpha, p_3\gamma)^{13}\text{C}$ corresponding to γ ray decays to the ground states of the corresponding nuclei with energies of $E_\gamma = 0.718, 3.089, 3.684,$ and 3.854 MeV.

The efficiency of the HPGe detector was determined with standard sources ^{60}Co and ^{137}Cs as well as the $^{27}\text{Al}(p, \gamma)^{28}\text{Si}$ reaction at the well known narrow resonance at $E_p = 992$ keV [62]. The detector was at a distance where geometric effects and summing could be neglected. In this way the uncertainty in the efficiency was determined to 6% for the γ ray energies of interest.

Prominent γ -ray lines were observed in the the HPGe spectrum at $E_\gamma = 3.089, 3.684,$ and 3.854 MeV, while the line at $E_\gamma = 0.718$ MeV was only observed weakly at a few energies. Therefore, the cross sections for the $^{10}\text{B}(\alpha, p_1\gamma)^{13}\text{C}$, $^{10}\text{B}(\alpha, p_2\gamma)^{13}\text{C}$, and $^{10}\text{B}(\alpha, p_3\gamma)^{13}\text{C}$ were extracted while that of the $^{10}\text{B}(\alpha, \alpha_1\gamma)^{10}\text{B}$ reaction was neglected.

In order to calculate the $^{10}\text{B}(\alpha, p_1\gamma)^{13}\text{C}$, $^{10}\text{B}(\alpha, p_2\gamma)^{13}\text{C}$, and $^{10}\text{B}(\alpha, p_3\gamma)^{13}\text{C}$ cross sections, the γ -ray decay branching ratios [63] must be considered. In addition, since the angular distributions of the secondary cascade γ rays are unknown, the differential cross sections measured at 130° are assumed to be proportional to the angle integrated cross section. This should be a reasonable approximation since secondary γ -ray angular distributions are symmetric about 90° and the second-order Legendre polynomial is small at this angle of observation. Under these approximations, the branching ratios can be simply multiplied by the efficiency corrected yields

TABLE I. Differential cross sections at 0° for the $^{10}\text{B}(\alpha, n)^{13}\text{N}$ reaction, in the laboratory frame of reference. The data have an overall systematic uncertainty of 12% as discussed in Sec. II.

E_α (keV)	σ (b/sr)	E_α (keV)	σ (b/sr)	E_α (keV)	σ (b/sr)	E_α (keV)	σ (b/sr)
575	$8.35(104) \times 10^{-9}$	1044	$1.89(22) \times 10^{-7}$	1304	$2.21(23) \times 10^{-6}$	1725	$9.33(103) \times 10^{-6}$
595	$7.06(91) \times 10^{-9}$	1050	$2.24(26) \times 10^{-7}$	1330	$2.93(30) \times 10^{-6}$	1735	$9.15(103) \times 10^{-6}$
615	$7.77(98) \times 10^{-9}$	1054	$2.49(30) \times 10^{-7}$	1354	$2.69(28) \times 10^{-6}$	1744	$8.59(98) \times 10^{-6}$
635	$8.15(102) \times 10^{-9}$	1060	$4.01(45) \times 10^{-7}$	1404	$3.61(44) \times 10^{-6}$	1755	$9.77(108) \times 10^{-6}$
655	$9.05(111) \times 10^{-9}$	1074	$3.44(36) \times 10^{-7}$	1421	$5.47(64) \times 10^{-6}$	1804	$2.01(24) \times 10^{-5}$
675	$1.14(13) \times 10^{-8}$	1080	$4.84(53) \times 10^{-7}$	1445	$9.09(102) \times 10^{-6}$	1855	$2.60(32) \times 10^{-5}$
694	$1.45(16) \times 10^{-8}$	1095	$6.83(78) \times 10^{-7}$	1454	$1.63(17) \times 10^{-5}$	1922	$3.21(35) \times 10^{-5}$
714	$1.45(16) \times 10^{-8}$	1100	$7.96(89) \times 10^{-7}$	1458	$1.32(14) \times 10^{-5}$	1922	$3.54(43) \times 10^{-5}$
734	$1.70(19) \times 10^{-8}$	1105	$1.04(11) \times 10^{-6}$	1554	$4.26(44) \times 10^{-5}$	1922	$3.63(43) \times 10^{-5}$
754	$1.60(18) \times 10^{-8}$	1110	$1.34(14) \times 10^{-6}$	1575	$2.53(28) \times 10^{-5}$	1962	$2.99(33) \times 10^{-5}$
774	$2.27(24) \times 10^{-8}$	1114	$1.32(14) \times 10^{-6}$	1604	$1.72(20) \times 10^{-5}$	1982	$2.81(32) \times 10^{-5}$
834	$3.30(34) \times 10^{-8}$	1115	$2.68(29) \times 10^{-6}$	1605	$2.06(22) \times 10^{-5}$	2022	$2.74(32) \times 10^{-5}$
854	$3.37(35) \times 10^{-8}$	1119	$1.29(13) \times 10^{-6}$	1615	$1.83(19) \times 10^{-5}$	2064	$3.77(45) \times 10^{-5}$
860	$3.82(40) \times 10^{-8}$	1130	$1.78(18) \times 10^{-6}$	1625	$2.17(23) \times 10^{-5}$	2082	$3.61(44) \times 10^{-5}$
865	$3.60(39) \times 10^{-8}$	1140	$1.43(15) \times 10^{-6}$	1630	$3.28(37) \times 10^{-5}$	2185	$2.14(22) \times 10^{-4}$
904	$5.44(56) \times 10^{-8}$	1150	$1.73(18) \times 10^{-6}$	1635	$4.08(47) \times 10^{-5}$	2203	$2.31(24) \times 10^{-4}$
924	$6.32(64) \times 10^{-8}$	1160	$1.43(15) \times 10^{-6}$	1645	$5.59(63) \times 10^{-5}$	2221	$3.13(32) \times 10^{-4}$
943	$7.07(72) \times 10^{-8}$	1170	$1.49(16) \times 10^{-6}$	1654	$2.47(30) \times 10^{-5}$	2222	$2.16(23) \times 10^{-4}$
964	$8.49(86) \times 10^{-8}$	1180	$1.00(11) \times 10^{-6}$	1655	$3.41(37) \times 10^{-5}$	2277	$5.45(55) \times 10^{-4}$
985	$9.91(101) \times 10^{-8}$	1185	$1.00(11) \times 10^{-6}$	1665	$1.76(21) \times 10^{-5}$	2296	$5.74(59) \times 10^{-4}$
1005	$1.16(11) \times 10^{-7}$	1185	$7.33(84) \times 10^{-7}$	1675	$8.12(92) \times 10^{-6}$	2305	$5.89(60) \times 10^{-4}$
1025	$1.33(13) \times 10^{-7}$	1205	$7.79(90) \times 10^{-7}$	1685	$8.86(100) \times 10^{-6}$	2322	$4.43(46) \times 10^{-4}$
1029	$1.72(21) \times 10^{-7}$	1224	$1.12(12) \times 10^{-6}$	1695	$1.33(14) \times 10^{-5}$	2404	$2.69(27) \times 10^{-4}$
1029	$1.55(19) \times 10^{-7}$	1244	$1.82(19) \times 10^{-6}$	1704	$1.11(12) \times 10^{-5}$	2421	$2.52(26) \times 10^{-4}$
1035	$1.74(22) \times 10^{-7}$	1264	$2.06(21) \times 10^{-6}$	1705	$1.18(13) \times 10^{-5}$	2505	$2.30(23) \times 10^{-4}$
1040	$2.28(27) \times 10^{-7}$	1284	$2.07(21) \times 10^{-6}$	1715	$9.66(108) \times 10^{-6}$	2522	$2.38(25) \times 10^{-4}$

TABLE II. Angular distribution measurements for the $^{10}\text{B}(\alpha, n)^{13}\text{N}$ reaction, in the laboratory frame of reference. Alpha particle energies are in units of MeV, cross sections are in b/sr. Cross sections are from the present work except those at $E_\alpha = 1.5$ MeV, which were measured as part of the experiment reported in Liu *et al.* [46]. The data have common systematic uncertainty of 12% as discussed in Sec. II.

E_α (keV)	Angle (degrees)	$d\sigma/d\Omega$ (b/sr)
1.160	0	$1.74(18) \times 10^{-6}$
	60	$1.49(15) \times 10^{-6}$
	110	$1.46(15) \times 10^{-6}$
	135	$1.63(16) \times 10^{-6}$
	155	$1.78(18) \times 10^{-6}$
1.500	20	$3.71(19) \times 10^{-4}$
	30	$6.13(31) \times 10^{-4}$
	40	$9.09(46) \times 10^{-4}$
	50	$1.11(6) \times 10^{-3}$
	60	$1.31(7) \times 10^{-3}$
	70	$1.47(7) \times 10^{-3}$
	80	$1.49(7) \times 10^{-3}$
	90	$1.44(7) \times 10^{-3}$
	100	$1.44(7) \times 10^{-3}$
	1.570	0
30		$5.96(61) \times 10^{-5}$
60		$9.15(93) \times 10^{-5}$
90		$7.62(76) \times 10^{-5}$
110		$7.77(78) \times 10^{-5}$
135		$4.64(47) \times 10^{-5}$
1.650	0	$3.24(33) \times 10^{-5}$
	30	$5.75(57) \times 10^{-5}$
	60	$5.94(61) \times 10^{-5}$
	90	$8.51(87) \times 10^{-5}$
	110	$1.61(16) \times 10^{-4}$
	135	$1.42(15) \times 10^{-4}$
	155	$9.01(92) \times 10^{-5}$

and either added or subtracted to the yields of the different transitions to correct for feeding in or out.

D. Differential cross section

After the yields were determined as described above, differential cross sections $\frac{d\sigma}{d\Omega}$ were determined by

$$\frac{d\sigma}{d\Omega} \approx \frac{dY/d\Omega}{N_p N_t \epsilon} \quad (4)$$

with the assumption that the target is thin enough compared to the widths of the observed resonances that the energy loss effects through the target are negligible (see Sec. II). Here N_p is the number of beam particles made incident on the target, N_t is the number of target nuclei, $\frac{dY}{d\Omega}$ are the differential yields, and ϵ is the efficiency. The number of beam particles was determined from the accumulated charge on the electrically isolated beam stop, which was found to be accurate to 3%. The number of target atoms was determined from the target thickness given in Sec. II. The efficiency for the HPGe detector and deuterated liquid scintillators is described in

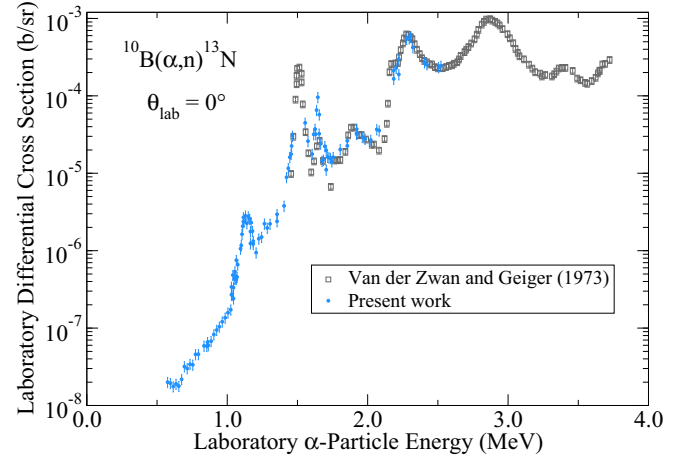


FIG. 7. Comparison between the present measurements (blue circles) and those of Van der Zwan and Geiger [13] (gray squares) at $\theta_{\text{lab}} = 0^\circ$ at low energy.

Secs. III C and III B respectively. The differential cross sections are given in Tables I, II, and III.

A comparison of the present $^{10}\text{B}(\alpha, n)^{13}\text{N}$ differential cross-section data at $\theta_{\text{lab}} = 0^\circ$ with that of Van der Zwan and Geiger [13] is shown in Fig. 7 and good agreement is observed over the overlapping energy range. In order to highlight the low-energy nuclear structure, the experimental data are converted to the differential S factor using

$$\frac{dS(E_{\text{c.m.}})}{d\Omega} = \frac{d\sigma(E_{\text{c.m.}})}{d\Omega} E_{\text{c.m.}} e^{2\pi\eta}, \quad (5)$$

where η is the Sommerfeld parameter that is given by

$$\eta = \frac{Z_1 Z_2 e^2}{\hbar} \sqrt{\frac{\mu}{2E_{\text{c.m.}}}}. \quad (6)$$

Here Z_1 and Z_2 are the charges of the entrance partition particles, μ is the reduced mass of the entrance partition particles, e is the elementary charge, and \hbar is the reduced

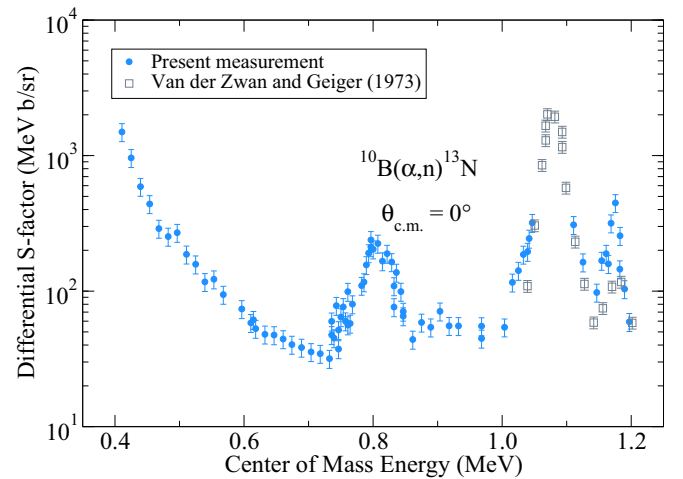


FIG. 8. Comparison between the lowenergy differential S factors of the present measurements (blue circles) and those of Van der Zwan and Geiger [13] (gray squares) at $\theta_{\text{lab}} = 0^\circ$.

TABLE III. Differential cross sections at 130° for the $^{10}\text{B}(\alpha, p_{1,2,3}\gamma)^{13}\text{C}$ reaction, in the laboratory frame of reference. The uncertainty in the α particle beam energy is ± 2 keV. The data have common systematic uncertainty of 8% as discussed in Sec. II.

E_α (MeV)	$d\sigma/d\Omega$ (b/sr)			E_α (MeV)	$d\sigma/d\Omega$ (b/sr)		
	$p_1\gamma$	$p_2\gamma$	$p_3\gamma$		$p_1\gamma$	$p_2\gamma$	$p_3\gamma$
0.835	$2.20(47) \times 10^{-7}$	$4.52(352) \times 10^{-8}$	$3.18(67) \times 10^{-7}$	1.140	$5.00(104) \times 10^{-5}$	$9.46(737) \times 10^{-6}$	$6.59(100) \times 10^{-4}$
0.855	$2.06(49) \times 10^{-7}$	$6.18(400) \times 10^{-8}$	$3.24(68) \times 10^{-7}$	1.150	$4.58(92) \times 10^{-5}$	$2.09(69) \times 10^{-5}$	$5.39(82) \times 10^{-4}$
0.860	$1.69(48) \times 10^{-7}$		$5.60(108) \times 10^{-7}$	1.160	$2.96(72) \times 10^{-5}$		$4.61(70) \times 10^{-4}$
0.865	$1.30(53) \times 10^{-7}$	$1.20(52) \times 10^{-7}$	$4.60(103) \times 10^{-7}$	1.170	$3.64(80) \times 10^{-5}$	$6.65(597) \times 10^{-6}$	$3.51(54) \times 10^{-4}$
0.905	$3.17(68) \times 10^{-7}$	$1.82(56) \times 10^{-7}$	$1.12(18) \times 10^{-6}$	1.180	$3.29(72) \times 10^{-5}$	$7.24(543) \times 10^{-6}$	$3.11(48) \times 10^{-4}$
0.925	$4.38(90) \times 10^{-7}$	$1.75(67) \times 10^{-7}$	$1.54(25) \times 10^{-6}$	1.185	$2.99(47) \times 10^{-5}$	$1.05(21) \times 10^{-5}$	$3.33(50) \times 10^{-4}$
0.944	$4.75(98) \times 10^{-7}$	$2.01(74) \times 10^{-7}$	$2.50(39) \times 10^{-6}$	1.185	$3.48(74) \times 10^{-5}$		$2.81(43) \times 10^{-4}$
0.965	$6.97(132) \times 10^{-7}$	$3.22(94) \times 10^{-7}$	$3.76(58) \times 10^{-6}$	1.206	$2.42(38) \times 10^{-5}$	$2.29(36) \times 10^{-5}$	$2.31(34) \times 10^{-4}$
0.985	$9.36(191) \times 10^{-7}$	$3.88(142) \times 10^{-7}$	$6.44(100) \times 10^{-6}$	1.225	$1.91(31) \times 10^{-5}$	$3.48(53) \times 10^{-5}$	$2.01(30) \times 10^{-4}$
1.005	$1.61(27) \times 10^{-6}$	$3.23(140) \times 10^{-7}$	$1.03(15) \times 10^{-5}$	1.245	$2.24(36) \times 10^{-5}$	$5.23(79) \times 10^{-5}$	$1.94(29) \times 10^{-4}$
1.025	$2.32(37) \times 10^{-6}$	$7.04(181) \times 10^{-7}$	$1.87(28) \times 10^{-5}$	1.265	$2.60(40) \times 10^{-5}$	$3.00(46) \times 10^{-5}$	$1.89(28) \times 10^{-4}$
1.030	$8.83(703) \times 10^{-7}$		$1.92(34) \times 10^{-5}$	1.285	$3.33(50) \times 10^{-5}$	$2.06(32) \times 10^{-5}$	$1.68(25) \times 10^{-4}$
1.030	$8.62(765) \times 10^{-7}$		$1.40(26) \times 10^{-5}$	1.305	$5.06(77) \times 10^{-5}$	$1.21(25) \times 10^{-5}$	$1.66(25) \times 10^{-4}$
1.035	$3.63(115) \times 10^{-6}$		$2.00(36) \times 10^{-5}$	1.330	$6.25(105) \times 10^{-5}$	$1.28(51) \times 10^{-5}$	$1.46(23) \times 10^{-4}$
1.040	$3.90(131) \times 10^{-6}$		$2.62(46) \times 10^{-5}$	1.355	$1.93(29) \times 10^{-4}$	$3.91(68) \times 10^{-5}$	$2.61(39) \times 10^{-4}$
1.045	$4.81(83) \times 10^{-6}$	$2.01(51) \times 10^{-6}$	$4.15(62) \times 10^{-5}$	1.355	$2.04(30) \times 10^{-4}$	$4.07(65) \times 10^{-5}$	$2.78(41) \times 10^{-4}$
1.045	$4.04(67) \times 10^{-6}$	$1.04(32) \times 10^{-6}$	$3.73(56) \times 10^{-5}$	1.405	$2.66(40) \times 10^{-4}$	$1.02(17) \times 10^{-4}$	$4.06(61) \times 10^{-4}$
1.045	$3.20(53) \times 10^{-6}$	$1.36(31) \times 10^{-6}$	$3.12(47) \times 10^{-5}$	1.422	$1.61(25) \times 10^{-4}$	$8.22(141) \times 10^{-5}$	$3.46(52) \times 10^{-4}$
1.045	$3.53(58) \times 10^{-6}$	$5.76(266) \times 10^{-7}$	$3.19(48) \times 10^{-5}$	1.446	$1.24(20) \times 10^{-4}$	$8.87(153) \times 10^{-5}$	$5.06(77) \times 10^{-4}$
1.050	$4.33(140) \times 10^{-6}$		$4.21(69) \times 10^{-5}$	1.455	$1.16(19) \times 10^{-4}$	$1.16(19) \times 10^{-4}$	$8.60(130) \times 10^{-4}$
1.055	$3.96(153) \times 10^{-6}$	$3.76(152) \times 10^{-6}$	$4.87(80) \times 10^{-5}$	1.458	$8.82(149) \times 10^{-5}$	$9.32(155) \times 10^{-5}$	$6.17(93) \times 10^{-4}$
1.060	$4.11(155) \times 10^{-6}$	$2.74(149) \times 10^{-6}$	$5.09(83) \times 10^{-5}$	1.555	$1.21(21) \times 10^{-4}$	$3.16(48) \times 10^{-4}$	$2.07(31) \times 10^{-3}$
1.065	$8.24(157) \times 10^{-6}$	$2.04(102) \times 10^{-6}$	$8.37(127) \times 10^{-5}$	1.575	$1.04(21) \times 10^{-4}$	$2.38(38) \times 10^{-4}$	$1.56(23) \times 10^{-3}$
1.065	$4.51(150) \times 10^{-6}$		$5.92(94) \times 10^{-5}$	1.605	$5.77(165) \times 10^{-5}$	$1.66(28) \times 10^{-4}$	$2.05(31) \times 10^{-3}$
1.070	$9.84(233) \times 10^{-6}$	$4.18(191) \times 10^{-6}$	$5.99(96) \times 10^{-5}$	1.605	$7.79(170) \times 10^{-5}$	$2.02(32) \times 10^{-4}$	$1.76(26) \times 10^{-3}$
1.075	$8.90(177) \times 10^{-6}$	$1.64(119) \times 10^{-6}$	$8.60(131) \times 10^{-5}$	1.616	$1.11(19) \times 10^{-4}$	$1.97(31) \times 10^{-4}$	$2.25(33) \times 10^{-3}$
1.080	$1.00(26) \times 10^{-5}$		$1.16(18) \times 10^{-4}$	1.625	$1.38(25) \times 10^{-4}$	$1.61(28) \times 10^{-4}$	$3.98(59) \times 10^{-3}$
1.095	$1.57(43) \times 10^{-5}$		$1.82(28) \times 10^{-4}$	1.630	$4.60(81) \times 10^{-4}$	$1.79(51) \times 10^{-4}$	$1.07(16) \times 10^{-2}$
1.100	$2.99(63) \times 10^{-5}$		$2.30(35) \times 10^{-4}$	1.636	$3.21(67) \times 10^{-4}$	$3.35(68) \times 10^{-4}$	$1.29(19) \times 10^{-2}$
1.105	$2.52(62) \times 10^{-5}$	$5.24(498) \times 10^{-6}$	$2.91(45) \times 10^{-4}$	1.645	$7.10(130) \times 10^{-4}$	$4.98(106) \times 10^{-4}$	$2.30(34) \times 10^{-2}$
1.110	$3.46(75) \times 10^{-5}$	$1.63(59) \times 10^{-5}$	$3.79(58) \times 10^{-4}$	1.655	$4.41(84) \times 10^{-4}$	$3.85(78) \times 10^{-4}$	$1.31(19) \times 10^{-2}$
1.115	$4.43(92) \times 10^{-5}$	$5.53(345) \times 10^{-6}$	$4.62(70) \times 10^{-4}$	1.656	$5.11(87) \times 10^{-4}$	$4.83(83) \times 10^{-4}$	$1.61(24) \times 10^{-2}$
1.120	$4.67(98) \times 10^{-5}$		$5.88(89) \times 10^{-4}$	1.665	$2.59(50) \times 10^{-4}$	$3.39(60) \times 10^{-4}$	$7.57(114) \times 10^{-3}$
1.130	$4.95(100) \times 10^{-5}$		$6.23(94) \times 10^{-4}$				

Plank's constant. The S factor for the present measurement of the $^{10}\text{B}(\alpha, n)^{13}\text{N}$ reaction is shown in Fig. 8.

The increasing slope in the S factor at low energies suggests the presence of a broad resonance at lower energy. The $^{10}\text{B}(\alpha, p_1\gamma)^{13}\text{C}$, $^{10}\text{B}(\alpha, p_2\gamma)^{13}\text{C}$, and $^{10}\text{B}(\alpha, p_3\gamma)^{13}\text{C}$ differential S factors at $\theta_{\text{lab}} = 130^\circ$ are shown in Fig. 10. The $^{10}\text{B}(\alpha, p_1\gamma)^{13}\text{C}$ and $^{10}\text{B}(\alpha, p_2\gamma)^{13}\text{C}$ also show an enhanced cross section at low energy, while the $^{10}\text{B}(\alpha, p_3\gamma)^{13}\text{C}$ cross section is described well by the previously observed higher energy resonance contributions.

IV. R-MATRIX ANALYSIS

The lowenergy cross sections of the $^{10}\text{B}(\alpha, n)^{13}\text{N}$ reaction have been analyzed in the framework of the phenomenological R -matrix approach [64,65] using the code AZURE2 [66,67]. The alternate parametrization of Brune [68] has been used in order to work directly with physical parameters and

to eliminate the need for boundary conditions. The physical constants used for the analysis of the ^{14}N system are given in Table IV. The present R -matrix fit required no background pole or subthreshold state contributions and can be reproduced with the parameters given in Table V. An AZURE2 input file is provided in the Supplemental Material [53] to facilitate the reproduction of the fit.

The $^{10}\text{B} + \alpha$ reactions populate the ^{14}N compound system above the α -particle [$S_\alpha = 11.61211(1)$], neutron [$S_n = 10.55338(27)$ MeV], proton [$S_p = 7.55056(1)$ MeV], and deuteron [$S_d = 10.2723080(7)$ MeV] separation energies [70,71], as shown in Fig. 9. In addition, the α -particle and proton deexcitations can populate excited states in ^{10}B [$E_x = 0.718380(11)$ MeV] and ^{13}C [$E_x = 3.089443(20)$, $3.684507(19)$, and $3.853807(19)$ MeV] respectively [72,73]. This allows for eight possible particle decay modes.

The proton and deuteron decay modes produce the stable nuclei ^{13}C and ^{12}C respectively. This corresponds to

TABLE IV. Channel radii and masses used for the R -matrix analysis of the ^{14}N system. Masses are taken from Wang *et al.* [69].

Parameter	Value	Unit
$a_c (^{10}\text{B} + \alpha)$	5	fm
$a_c (^{13}\text{C} + p)$	5	fm
$a_c (^{13}\text{N} + n)$	5	fm
$a_c (^{12}\text{C} + d)$	5	fm
M_p	1.00783	u
M_n	1.00866	u
M_α	4.00260	u
M_d	2.01410	u
$M_{^{10}\text{B}}$	10.0129	u
$M_{^{13}\text{C}}$	13.0034	u
$M_{^{13}\text{N}}$	13.0057	u
$M_{^{12}\text{C}}$	12	u

the $^{13}\text{C} + p$ and the $^{12}\text{C} + d$ reaction channels. For $^{13}\text{C} + p$ reactions, the proton separation energy is about 4 MeV lower

in energy than the α -particle separation energy. There are only a few $^{13}\text{C} + p$ measurements that extend over the same excitation energy range [17,18] ($4.4 < E_p < 5.7$ MeV) as the present $^{10}\text{B} + \alpha$ data. The deuteron separation energy is only about 1.3 MeV below the α -separation energy, and many measurements have been made over the overlapping excitation energy range for the $^{12}\text{C}(d, d)^{12}\text{C}$, $^{12}\text{C}(d, p)^{13}\text{C}$, and $^{12}\text{C}(d, n)^{13}\text{N}$ reactions [19–45] ($1.6 < E_d < 3.0$ MeV). While several of the resonances that have been observed in the $^{10}\text{B} + \alpha$ data have also been observed in the $^{13}\text{C} + p$ and $^{12}\text{C} + d$ data, many additional resonances have also been observed in these reactions over a similar excitation energy range. Because of the added complexity of these additional resonances, the current analysis does not consider the $^{13}\text{C} + p$ and $^{12}\text{C} + d$ data. The fit is also limited to $E_\alpha < 1.71$ MeV.

There are few measurements of the low-energy cross sections of the $^{10}\text{B} + \alpha$ reactions and even fewer that have data that can be accurately obtained. A very complete study was made by Shire *et al.* [8] but no data points were presented,

TABLE V. R -matrix parameters for the analysis of the ^{14}N system. The partial widths are in units of keV and excitation energies in MeV. The sign of the partial width indicates the interference sign of the corresponding reduced width amplitude.

J^π	E_x (this work)		This work/literature [8]									
	E_x [72]	l	s	Γ_α	Γ_n	Γ_{p0}	Γ_{p1}	Γ_{p2}	Γ_{p3}	Γ_d	Γ_{total}	
$(l \leq 2)^a$	$\leq 12^b$	1	3	4.0×10^{-5}							44	
		2	1			-6.1						
		1	1					-26				
		0	2						12			
4^-	12.421 12.418(3)	3	1	0.37							43/43(4)	
		4	0			0.047						
		4	0				0.38					
		3	1					2.4				
		2	2						0.54			
		1	3							27		
1^+	12.498 12.495(9)	3	1							11	36/36(5)	
		2	3	0.089								
		1	0			0.063						
		1	0				5.5					
		1	1					17				
2	2						13					
3^+	12.600 12.594(3)	0	3	0.53							66/50(5)	
		3	0			0.019						
		3	0				0.005					
		2	1					26				
		1	2						3.9			
		0	3							28		
		2	1									-7.2
3^-	12.689 12.690(5)	1	3	5.9/1.7							18/14(4)	
		2	1			-1.9/4.3						
		2	1				0.28/0.62					
		3	0					0.27/0.17				
		1	1						1.9/0.7			
		1	2							-7.2/5.6		
	3	1							0.43/0.93			

^aThe penetrability of the α -channel constrains this state to a relative orbital angular momentum of less than or equal to 2. For the present analysis a spin-parity of 2^- has been used. See Sec. V for further discussion.

^bThe excitation energy of this level was fixed at $E_x = 12$ MeV, representing an upper limit on the level energy imposed by the data.

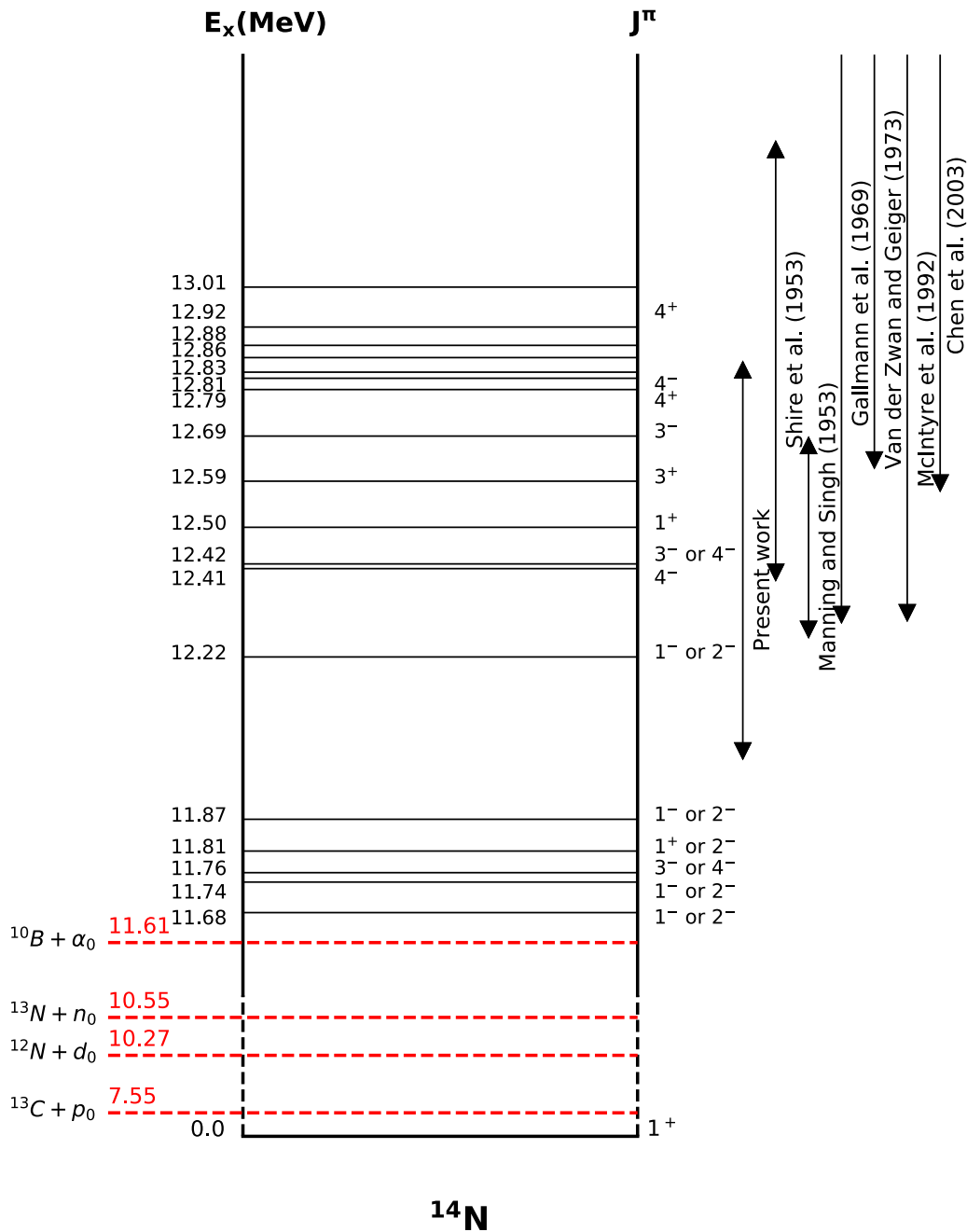


FIG. 9. Level diagram of the ^{14}N system with level information near the α -particle separation energy pertinent to the present analysis.

only lines that represented the general trend of the data. This results in a large and rather difficult to quantify uncertainty in the digitization of the data. Manning and Singh [10] measured only the $^{10}\text{B}(\alpha, p_0)^{13}\text{C}$ cross section, but to even lower energy than Shire *et al.* [8], reporting an additional weak narrow resonance at about $E_\alpha = 1$ MeV. Van der Zwan and Geiger [13] made a study of the differential cross section at three angles of $\theta_{\text{lab}} = 0^\circ, 90^\circ$, and 160° , but their measurements only extend over the strong resonance at $E_\alpha = 1.51$ MeV (see Fig. 7). Similarly, the $^{10}\text{B}(\alpha, p_0)^{13}\text{C}$ data of Chen *et al.* [14] also extend just below this same resonance. McIntyre *et al.* [16] has made the lowest energy study of

the $^{10}\text{B}(\alpha, \alpha)^{10}\text{B}$ reaction, but only the highest energy resonance considered in the R -matrix analysis can be observed. No previous $^{10}\text{B}(\alpha, \alpha_1)^{10}\text{B}$ measurements have been reported over this energy region, and the present measurements confirm that the cross section is small over the range of the R -matrix analysis.

Because of the limited data for the different decay modes, those of Shire *et al.* [8] have been digitized from Fig. 2 of that work. Because no actual data points are shown, only a line, points were digitized using a spacing that reflects the change in cross section as a function of energy. For the fitting, uncertainties of 20% were arbitrarily assigned. The inclusion of this

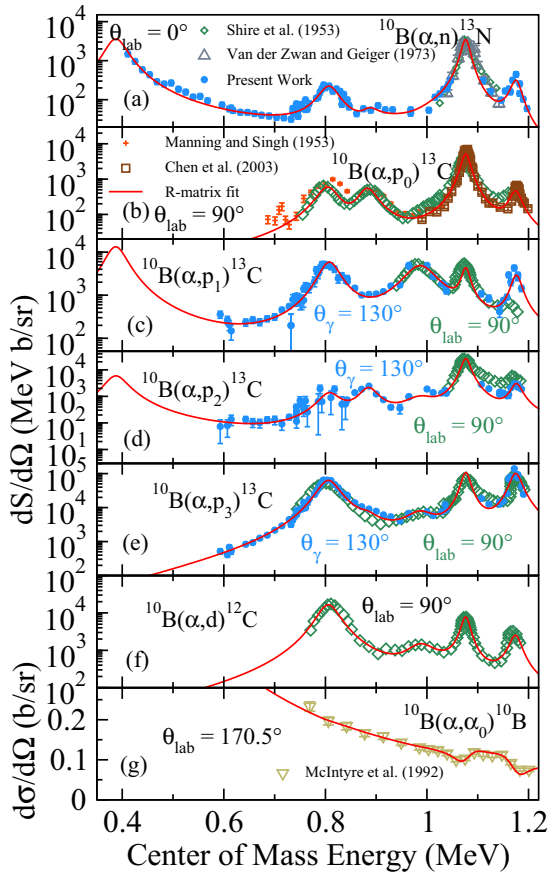


FIG. 10. Comparison of the present $^{10}\text{B} + \alpha$ measurements (blue circles) with those measured previously (Shire *et al.* [8] (green diamonds), Manning and Singh [10] (orange crosses), Van der Zwan and Geiger [13] (grey upward triangles), Chen *et al.* [14] (brown squares), and McIntyre *et al.* [16] (khaki downward triangles)) at low energy. The red solid curve represents the R -matrix fit described in the text and the calculation and is shown at 0° , 90° , 130° , 130° , 130° , 90° , and 170.5° for the reactions $^{10}\text{B}(\alpha, n)^{13}\text{N}$ (a), $^{10}\text{B}(\alpha, p_0)^{13}\text{C}$ (b), $^{10}\text{B}(\alpha, p_1)^{13}\text{C}$ (c), $^{10}\text{B}(\alpha, p_2)^{13}\text{C}$ (d), $^{10}\text{B}(\alpha, p_3)^{13}\text{C}$ (e), $^{10}\text{B}(\alpha, d)^{12}\text{C}$ (f), and $^{10}\text{B}(\alpha, \alpha)^{10}\text{B}$ (g) respectively.

data added significant constraint to the R -matrix analysis by providing data over two additional lower energy resonances in the $^{10}\text{B}(\alpha, p_0)^{13}\text{C}$ reaction and providing the only data for the $^{10}\text{B}(\alpha, d)^{12}\text{C}$ reaction, as shown in Fig. 10.

Comparisons of the present $^{10}\text{B} + \alpha$ data with excitation curves from Shire *et al.* [8], Manning and Singh [10], Chen *et al.* [14], Van der Zwan and Geiger [13] and McIntyre *et al.* [16] are shown in Fig. 10. In order to highlight the nuclear contribution of the cross section, the data are plotted as differential astrophysical S factor. The data are limited to measurements at only a few angles, so there is limited constraint on the spin-parities of the states. Those values reported in the compilation [72] have been utilized, which were largely determined by the angular distribution studies of Shire *et al.* [8]. Unfortunately Shire *et al.* [8] only report angular distribution coefficients with no angular distribution data.

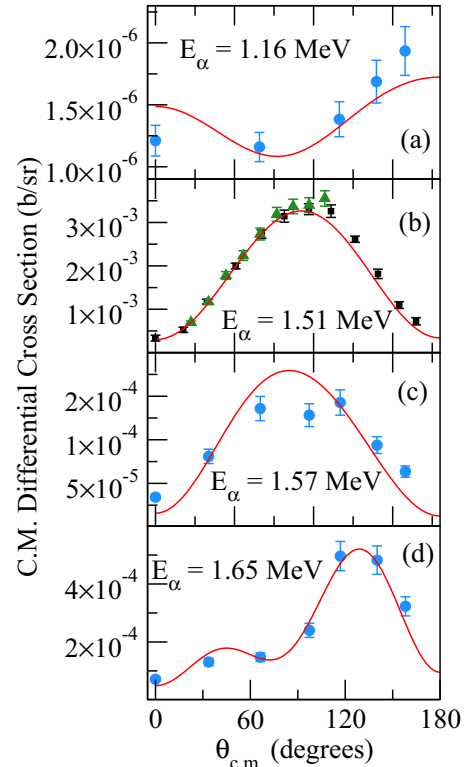


FIG. 11. Angular distribution measurements of the $^{10}\text{B}(\alpha, n)^{13}\text{N}$ reaction for $E_\alpha < 1.71$ MeV at 1.16 (a), 1.51 (b), 1.57 (c), and 1.65 MeV (d). The data of the present work are indicated by blue circles, those of Van der Zwan and Geiger [13] by black squares, and those of Liu *et al.* [46] by green triangles. The red solid line represents the R -matrix fit.

Only a single angular distribution measurement for the $^{10}\text{B}(\alpha, n)^{13}\text{N}$ reaction is available from Van der Zwan and Geiger [13] for the strong resonance at $E_\alpha = 1.51$ MeV. An angular distribution measurement of this same resonance was also made in the experiment of Liu *et al.* [46], but was not reported in that work as it was below the energy range of interest. In addition, three angular distribution measurements were made as part of this work at $E_\alpha = 1.16$, 1.57, and 1.65 MeV. These data were included in the R -matrix fit and are shown in Fig. 11.

A generally consistent R -matrix fit was found that could reproduce the data of Shire *et al.* [8], Chen *et al.* [14], Van der Zwan and Geiger [13], and McIntyre *et al.* [16] as well as those of the present measurement. The $^{10}\text{B}(\alpha, p_0)^{13}\text{C}$ data of Manning and Singh [10] are somewhat discrepant from those of Shire *et al.* [8] over their region of overlap, most notably for the three data points in the vicinity of the resonance at $E_{\text{c.m.}} \approx 0.8$ MeV. This may be the result of energy averaging effects from their target of $5 \mu\text{g}/\text{cm}^2$, but, in attempting to perform the target effect correction, it was found that a target of approximately three times the quoted thickness was necessary to reproduce the data. Further, the data near $E_{\text{c.m.}} = 0.71$ MeV indicate an additional low-energy resonance. No other experimental measurements have observed a state at this energy. Therefore, the data of Manning and Singh [10]

TABLE VI. Summary of excitation curve data sets that were included or excluded for the R matrix. Details are discussed in the text. If the data are not considered in the fit, the χ^2 represents a calculation based on the parameters from the best fit. Here N is the number of data points in the data set.

Ref.	Reaction	θ_{lab} (deg.)	χ^2	N
Shire <i>et al.</i> [8]	$^{10}\text{B}(\alpha, n)^{13}\text{N}$	0°	66^{a}	31
	$^{10}\text{B}(\alpha, p_0)^{13}\text{C}$	90°	113^{a}	63
	$^{10}\text{B}(\alpha, p_1)^{13}\text{C}$	90°	29^{a}	38
	$^{10}\text{B}(\alpha, p_2)^{13}\text{C}$	90°	15^{a}	20
	$^{10}\text{B}(\alpha, p_3)^{13}\text{C}$	90°	109^{a}	53
	$^{10}\text{B}(\alpha, d)^{12}\text{C}$	90°	53^{a}	55
Van der Zwan and Geiger [13]	$^{10}\text{B}(\alpha, n)^{13}\text{N}$	0°	41^{b}	13
		90°	21^{b}	14
McIntyre <i>et al.</i> [16]	$^{10}\text{B}(\alpha, \alpha)^{10}\text{B}$	170.5°	29^{c}	22
Chen <i>et al.</i> [14]	$^{10}\text{B}(\alpha, p_0)^{13}\text{C}$	90°	123^{d}	44
this work	$^{10}\text{B}(\alpha, n)^{13}\text{N}$	0°	154	81
	$^{10}\text{B}(\alpha, p_1\gamma)^{13}\text{C}$	130°	77	67
	$^{10}\text{B}(\alpha, p_2\gamma)^{13}\text{C}$	130°	85	53
	$^{10}\text{B}(\alpha, p_3\gamma)^{13}\text{C}$	130°	95	67

^aDigitized from a line. The number of points was chosen to give a good representation of the change in the cross section as a function of energy.

^bAn uncertainty of 20% was assumed.

^cA target convolution effect of 15 keV was included.

^dData were shifted 2 keV higher in energy.

have not been included in the R -matrix fit, but are included in Fig. 10 for comparison. The data of Gallmann *et al.* [11] were also investigated, but this data had to be digitized from Fig. 2 of that work. Because of the scale of the figure and the low yield at the energies of interest, the digitization could not be performed accurately and the resulting data had very large uncertainties ($\approx 50\%$) indicated by the large scatter in the data points. Given this complication, these data were also not included in the R -matrix fit. A summary of the data that were used for the R -matrix fit are given in Tables VI and VII and the R -matrix parameters are given in Table V.

V. DISCUSSION

The present measurements of the $^{10}\text{B}(\alpha, n)^{13}\text{N}$ reaction extend to a previously unobserved energy range of $E_{\text{c.m.}} < 1.0$ MeV ($E_\alpha < 1.4$ MeV) (see Fig. 7). An R -matrix analysis was performed as described in Sec. IV, but it should be

TABLE VII. Summary of angular distribution data considered in the R -matrix fit. See Table VI.

Ref.	Reaction	E_α (MeV)	χ^2	N
Van der Zwan and Geiger [13]	$^{10}\text{B}(\alpha, n)^{13}\text{N}$	1.51	18	12
Liu <i>et al.</i> [46]	$^{10}\text{B}(\alpha, n)^{13}\text{N}$	1.50	5.2	9
this work	$^{10}\text{B}(\alpha, n)^{13}\text{N}$	1.16	7.7	5
		1.57	65	7
		1.65	20	7

emphasized that the limited amount of data available do not provide enough constraint for a unique solution. This means that the partial widths given in Table V should be taken as tentative values. The fit produces total widths that are in good agreement with Shire *et al.* [8], but there are discrepancies between the partial widths of the 3^- level at $E_x = 12.69$ MeV ($E_\alpha = 1.51$ MeV). Since the present fit must utilize the data of Shire *et al.* [8] for transitions that were not observed in the present measurements, an uncertainty analysis has not been performed given the lack of uncertainty information for that data. Measurements are under way for the charged particle producing $^{10}\text{B} + \alpha$ cross sections over a similar energy range, and an uncertainty analysis will be performed with the future publication of this data.

In addition to the previously observed strong resonance at $E_{\text{c.m.}} = 1.08$ MeV ($E_\alpha = 1.51$ MeV), new features are observed in the 0° $^{10}\text{B}(\alpha, n)^{13}\text{N}$ differential cross section. A weak structure has been observed at $E_{\text{c.m.}} \approx 0.89$ MeV ($E_\alpha = 1.24$ MeV), which can be reproduced by the weak population of the resonances that correspond to the states at $E_x = 12.50$ and 12.60 MeV (see partial widths in Table V). There is a clear but weak resonance at $E_{\text{c.m.}} \approx 0.806$ MeV ($E_\alpha = 1.13$ MeV), which is in good agreement with the level reported previously at $E_x = 12.418(3)$ MeV [72]. This level corresponds to resonances observed in all the other channels considered in the fit, as shown in Fig. 10.

There is also strong evidence for a broad lower energy resonance as indicated by the sharp rise in the S factor of the $^{10}\text{B}(\alpha, n)^{13}\text{N}$ reaction at low energies. The present data extend down to $E_{\text{c.m.}} = 411$ keV ($E_x = 12.023$ MeV) showing no decrease in the slope of the S factor, indicating that only the high-energy tail of the resonance has been observed. When the level energy is allowed to vary in the R -matrix fit, the lowest χ^2 is found when the excitation energy of the level is at an energy just lower than the lowest energy data point. However, this χ^2 dependence is weak and similar fits can be obtained with the level at a lower excitation energy. The fact that only the tail has been observed results in a large uncertainty for the level energy, which can only be resolved by further experimental efforts towards lower energies. In addition, both the $^{10}\text{B}(\alpha, p_1\gamma)^{13}\text{C}$ and $^{10}\text{B}(\alpha, p_2\gamma)^{13}\text{C}$ S factors flatten out at the lowest energies, further suggesting the presence of a lower energy resonance contribution (see Fig. 10).

Considering the large strength in the α channel necessary to explain such resonance phenomenon, the state is likely to be characterized by an α -cluster configuration. The emergence of such pronounced α -cluster resonance near the threshold is a well known phenomena which has been summarized by Ikeda *et al.* [74] for even-even nuclei. In more general terms, the appearance of such phenomena are explained as a genuine consequence of continuum coupling in the open quantum system (OQS) description of nuclear many-body system. The coupling of shell model (SM) eigenstates via the open particle decay channel leads to the formation of the aligned OQS eigenstate, which captures most of the continuum coupling and is an archetype of the cluster state [75]. Such α -cluster configurations are expected to have a pronounced α strength but largely reduced single-particle strengths.

Previous efforts provide some possible candidate states that could correspond to this low-energy resonance. There are three broad levels reported in the compilation at nearby excitation energies to which this resonance could correspond. The level reported at $E_x = 12.200(19)$ MeV ($E_\alpha = 0.823$ MeV) has a total width of $\Gamma = 300(30)$ keV, but the present data indicate that the resonance peak should be lower in energy ($E_x \leq 12.0$ MeV or $\leq E_\alpha = 0.54$ MeV). Two other candidates are the levels reported at $E_x = 11.874(6)$ MeV ($E_\alpha = 0.366$ MeV) or $E_x = 11.807(7)$ MeV ($E_\alpha = 0.273$ MeV) with widths of $\Gamma = 101(9)$ and $119(9)$ keV respectively [72].

Besides those levels reported in the most recent compilation [72], an earlier version, by Ajzenberg-Selove [76], indicated a level at $E_x = 11.95(3)$ MeV ($E_\alpha = 0.473$ MeV) ($J^\pi = 2^+$) that was deduced from measurements of the transfer reactions $^{12}\text{C}(^3\text{He}, p)^{14}\text{N}$ [77], $^{12}\text{C}(^6\text{Li}, \alpha)^{14}\text{N}$ [78], and $^{15}\text{N}(p, d)^{14}\text{N}$ [79]. However, it was dropped from the compilation at some point, likely because subsequent experiments failed to observe it. In addition, a level has been observed at $E_x = 11.956(5)$ MeV ($E_\alpha = 0.481$ MeV) with a high resolution (≈ 30 keV) $^{10}\text{B}(^6\text{Li}, d)^{14}\text{N}$ measurement, but the results have not been published [80].

There has also been a level reported at $E_x = 11.925$ MeV ($E_\alpha = 0.438$ MeV) ($\Gamma = 61$ keV) or 11.923 MeV ($E_\alpha = 0.435$ MeV) ($\Gamma = 87$ keV) by Gmür and Müller [30], which was observed in the $^{12}\text{C}(d, p_0)^{13}\text{C}$ and $^{12}\text{C}(d, n_0)^{13}\text{N}$ reactions, respectively. However, this state does not present itself as a clear peak in those cross sections and is largely masked by the tail contributions of other much stronger nearby resonances. A detailed R -matrix fit of the $^{12}\text{C} + d$ reactions is likely necessary in order to confirm the presence of this level.

In the present analysis, the rise in cross section is reproduced by the lowest energy level given in Table V. Given that the current $^{10}\text{B}(\alpha, n)^{13}\text{N}$ measurements have only been made at a single angle of 0° , the J^π of the corresponding state is not well constrained. The lowest energy angular distribution measured in this work at $E_\alpha = 1.16$ MeV does give some constraint on the J^π of this resonance. The observed strength of the resonance in the 0° differential cross section limits the entrance channel penetrability to values $l \leq 2$. This limits the possible J^π values to 1^+ , 2^- , 2^+ , 3^- , 3^+ , 4^- , 4^+ , and 5^+ . In addition, if this same resonance is also responsible for the increasing trend in the S factor of the $^{10}\text{B}(\alpha, p_1)^{13}\text{C}$ and $^{10}\text{B}(\alpha, p_2)^{13}\text{C}$ cross sections, the relative angular momentum in this channels must be $l \leq 3$. This further limits the J^π values to 1^+ , 2^- , 2^+ , 3^- , 3^+ , and 4^- . The angular distribution at $E_\alpha = 1.16$ MeV gives further constraint because the R -matrix fit indicates that there is significant interference between the tail of this low-energy resonance and the weakly populated (at least at 0°) resonance at $E_\alpha = 1.13$ MeV. Given that the J^π of the $E_\alpha = 1.13$ MeV ($E_x = 12.42$ MeV) is correctly assigned, the J^π that gave the best fit for this low-energy resonance is 2^- . With these considerations, a tentative assignment of 2^- is made for this new low-energy resonance.

VI. REACTION RATE

From the R -matrix analysis in Sec. IV, the angle integrated cross sections were calculated from the fitted differential cross

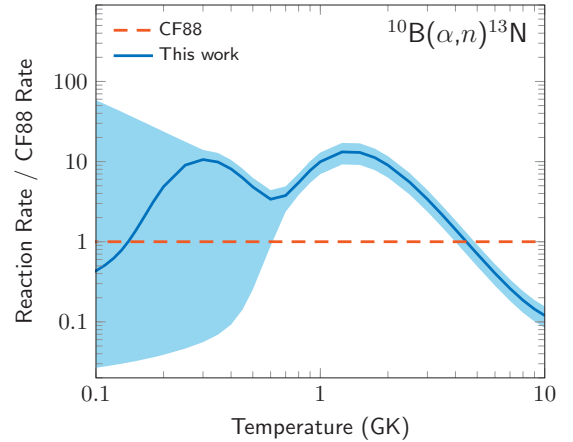


FIG. 12. Comparison of the $^{10}\text{B}(\alpha, n)^{13}\text{N}$ reaction rate to that of CF88 [82]. The solid blue line represents the ratio of the rate from the present work to that of CF88, while the light blue region represents the uncertainty range as described in the text. The red dashed line represents the ratio of CF88 to itself for reference.

sections. The accuracy of this assumption is difficult to quantify as limited angular distribution information is available. However, there were no issues obtaining a reasonable representation of the data, including the few angular distributions that are available, using the spin-parity assignments from the literature [8,72] for levels populated in the experiment. Further, as is shown below, the main contributors to the reaction rate are from the previously observed strong resonance at $E_\alpha = 1.51$ MeV and from the newly proposed strong low-energy resonance. Angular distribution measurements are available from Van der Zwan and Geiger [13] and Liu *et al.* [46] for this resonance and they are in good agreement with R -matrix fit, as shown in Fig. 11. The uncertainty estimated in the region of the new low-energy resonance are discussed below.

The $^{10}\text{B}(\alpha, n)^{13}\text{N}$ reaction rate has not been re-investigated since Harris *et al.* [81]. The same rate is given without modification by Caughlan and Fowler [82] (CF88). It is based on the extrapolation of the thick-target data of Roughton *et al.* [83] and does not take into account any of the low-energy resonance structure of the cross section. Figure 12 illustrates the recommended value (solid blue line) and uncertainty (light blue shaded region) of the reaction rate compared to that of CF88. As the uncertainties are dominated by systematic ones with unknown underlying probability density functions, the uncertainty band represents upper and lower limits, not a statistical range.

The upper-limit band at low temperatures, below 0.25 GK, has been determined by placing a single strong resonance at low energy with an α -particle reduced width amplitude equal to the Wigner limit ($l = 0$). Transfer studies indicate that it is unlikely a state exists with such a large reduced width, but this serves as a reasonable upper limit estimate given the paucity of information. At higher temperatures, the uncertainty is dominated by the overall systematic uncertainty in the cross-section measurements of $\pm 30\%$.

TABLE VIII. Reaction rate and lower and upper limits determined in this work.

T (GK)	$N_A \langle \sigma v \rangle$ ($\text{cm}^3 \text{mol}^{-1} \text{s}^{-1}$)		
	Recommended value	Upper limit	Lower limit
0.1	1.6×10^{-13}	2.1×10^{-11}	9.6×10^{-15}
0.11	1.1×10^{-12}	1.2×10^{-10}	6.2×10^{-14}
0.12	7.0×10^{-12}	5.2×10^{-10}	3.2×10^{-13}
0.13	3.7×10^{-11}	2.0×10^{-9}	1.4×10^{-12}
0.14	1.8×10^{-10}	6.6×10^{-9}	5.4×10^{-12}
0.15	7.7×10^{-10}	2.0×10^{-8}	1.8×10^{-11}
0.16	3.0×10^{-9}	5.3×10^{-8}	5.6×10^{-11}
0.18	3.5×10^{-8}	3.0×10^{-7}	4.0×10^{-10}
0.2	2.8×10^{-7}	1.4×10^{-6}	2.2×10^{-9}
0.25	1.4×10^{-5}	2.7×10^{-5}	7.1×10^{-8}
0.3	2.0×10^{-4}	2.6×10^{-4}	1.0×10^{-6}
0.35	1.3×10^{-3}	1.7×10^{-3}	9.4×10^{-6}
0.4	5.7×10^{-3}	7.4×10^{-3}	6.5×10^{-5}
0.45	1.8×10^{-2}	2.3×10^{-2}	4.0×10^{-4}
0.5	4.4×10^{-2}	5.8×10^{-2}	2.3×10^{-3}
0.6	2.2×10^{-1}	2.9×10^{-1}	5.7×10^{-2}
0.7	1.2×10^0	1.5×10^0	7.3×10^{-1}
0.8	6.1×10^0	7.9×10^0	4.3×10^0
0.9	2.5×10^1	3.3×10^1	1.8×10^1
1	8.3×10^1	1.1×10^2	5.8×10^1
1.25	7.0×10^2	9.0×10^2	4.9×10^2
1.5	2.8×10^3	3.6×10^3	2.0×10^3
1.75	7.3×10^3	9.5×10^3	5.1×10^3
2	1.5×10^4	1.9×10^4	1.0×10^4
2.5	3.7×10^4	4.8×10^4	2.6×10^4
3	6.6×10^4	8.6×10^4	4.6×10^4
3.5	9.7×10^4	1.3×10^5	6.8×10^4
4	1.3×10^5	1.6×10^5	8.8×10^4
5	1.7×10^5	2.2×10^5	1.2×10^5
6	2.0×10^5	2.6×10^5	1.4×10^5
7	2.2×10^5	2.9×10^5	1.6×10^5
8	2.3×10^5	3.0×10^5	1.6×10^5
9	2.4×10^5	3.1×10^5	1.7×10^5
10	2.4×10^5	3.1×10^5	1.7×10^5

The lower-limit band at low temperatures, below 0.8 GK, is calculated from the R -matrix fit obtained in Sec. IV but excluding the newly proposed low-energy resonance. This is essentially the reaction rate that could have been calculated with the data of Shire *et al.* [8] (1953). Again at higher

temperature the uncertainty is dominated by the systematic uncertainty in the cross section. The recommended value of the reaction rate, along with the upper and lower limits, is given in Table VIII.

VII. SUMMARY

New measurements have been presented for the low-energy differential cross section of the $^{10}\text{B}(\alpha, n)^{13}\text{N}$ reaction at $\theta_{\text{lab}} = 0^\circ$ and the $^{10}\text{B}(\alpha, p_{1,2,3}\gamma)^{13}\text{C}$ reactions at $\theta_\gamma = 130^\circ$. Measurements of these cross sections extend to lower energies than previously reported studies, and new resonances have been observed. An R -matrix analysis, which considers all of the existing $^{10}\text{B} + \alpha$ data below $E_\alpha = 1.71$ MeV, but currently neglects the $^{12}\text{C} + d$ and $^{13}\text{C} + p$ data, finds reasonable consistency between the different $^{10}\text{B} + \alpha$ measurements. A survey of the measurements in the literature finds that re-measurements of other decay channels is in order. The new data strongly suggest the presence of new strong low-energy resonance, but, since only the tail has been observed in the present data, the energy of this resonance remains uncertain. Indirect studies have reported several possible levels that could be candidates for this resonance as well as others at even lower energies. For this reason the rate of the $^{10}\text{B}(\alpha, n)^{13}\text{N}$ reaction remains highly uncertain below 0.7 GK. As the temperature range of interest for primordial stars extends down to approximately 0.2 GK, the reaction will be further studied at lower energies at the new CASPAR underground facility [84].

ACKNOWLEDGMENTS

This research utilized resources from the Notre Dame Center for Research Computing and was supported by the National Science Foundation through Grant No. Phys-1713857 and the Joint Institute for Nuclear Astrophysics through Grants No. Phys-0822648 and No. PHY-1430152 (JINA Center for the Evolution of the Elements). This material is based upon work supported by the U.S. Department of Energy, Office of Science, Office of Nuclear Physics, under Grant No. DE-AC05-00OR22725.

The authors would like to thank the NIST Center for Neutron Research (NCNR) for their technical support. Partial funding for this research was provided by the United States National Research Council. Contributions to this article by workers at the National Institute of Standards and Technology, an agency of the U.S. Government, are not subject to copyright.

-
- [1] M. Wiescher, J. Görres, and H. Schatz, *J. Phys. G: Nucl. Part. Phys.* **25**, R133 (1999).
[2] J. Bahcall, *Sci. Am.* **221**, 28 (1969).
[3] A. Heger and S. E. Woosley, *Astrophys. J.* **567**, 532 (2002).
[4] R. J. deBoer, J. Görres, M. Wiescher, R. E. Azuma, A. Best, C. R. Brune, C. E. Fields, S. Jones, M. Pignatari, D. Sayre, K. Smith, F. X. Timmes, and E. Uberseder, *Rev. Mod. Phys.* **89**, 035007 (2017).
[5] A. Frebel and J. E. Norris, *Annu. Rev. Astron. Astrophys.* **53**, 631 (2015).
[6] S. C. Keller, M. S. Bessell, A. Frebel, A. R. Casey, M. Asplund, H. R. Jacobson, K. Lind, J. E. Norris, D. Yong, A. Heger, Z. Magic, G. S. Da Costa, B. P. Schmidt, and P. Tisserand, *Nature (London)* **506**, 463 (2014).
[7] M. Wiescher, J. Görres, S. Graff, L. Buchmann, and F.-K. Thielemann, *Astrophys. J.* **343**, 352 (1989).

- [8] E. Shire, J. Wormald, G. Lindsay-Jones, A. Lundén, and A. Stanley, *Philos. Mag.* **44**, 1197 (1953).
- [9] E. Shire and R. Edge, *Philos. Mag.* **46**, 640 (1955).
- [10] G. Manning and B. Singh, *Proc. Phys. Soc. Sect. A* **66**, 842 (1953).
- [11] A. Gallmann, F. Hibou, and P. Fintz, *Nucl. Phys. A* **123**, 27 (1969).
- [12] A. Stanley, *London Dublin Edinburgh Philos. Mag. J. Sci.* **45**, 430 (1954).
- [13] L. Van der Zwan and K. Geiger, *Nucl. Phys. A* **216**, 188 (1973).
- [14] H. Chen, X. Wang, L. Shao, J. Liu, A. Yen, and W. Kan Chu, *Nucl. Instrum. Methods Phys. Res., Sect. B* **211**, 1 (2003).
- [15] F. L. Talbott and N. P. Heydenburg, *Phys. Rev.* **90**, 186 (1953).
- [16] L. McIntyre, J. Leavitt, M. Ashbaugh, Z. Lin, and J. Stoner, *Nucl. Instrum. Methods Phys. Res., Sect. B* **64**, 457 (1992).
- [17] E. Kashy, R. R. Perry, R. L. Steele, and J. R. Risser, *Phys. Rev.* **122**, 884 (1961).
- [18] P. Dagley, W. Haerberli, and J. Saladin, *Nucl. Phys.* **24**, 353 (1961).
- [19] M. Allab, M. Amiel, A. Amokrane, H. Beaumevieille, A. Henni, and M. Lambert, *J. Phys. France* **31**, 919 (1970).
- [20] T. W. Bonner, J. T. Eisinger, A. A. Kraus, and J. B. Marion, *Phys. Rev.* **101**, 209 (1956).
- [21] I. Borbély, T. Dolinszky, J. Erő, and G. Hrehuss, *Acta Phys. Acad. Sci. Hung.* **26**, 269 (1969).
- [22] L. F. Chase, R. G. Johnson, and E. K. Warburton, *Phys. Rev.* **120**, 2103 (1960).
- [23] G. Debras and G. Deconninck, *J. Radioanal. Chem.* **38**, 193 (1977).
- [24] A. Elwyn, J. V. Kane, S. Ofer, and D. H. Wilkinson, *Phys. Rev.* **116**, 1490 (1959).
- [25] F. Pierre, *Ann. Phys. (NY)* **13**, 435 (1965).
- [26] A. Gallmann, P. Fintz, and P. Hodgson, *Nucl. Phys.* **82**, 161 (1966).
- [27] L. Csedreki, I. Uzonyi, G. Á. Szíki, Z. Szikszai, G. Gyürky, and Á. Kiss, *Nucl. Instrum. Methods Phys. Res., Sect. B* **328**, 59 (2014).
- [28] N. Davison, P. Fintz, and A. Gallmann, *Nucl. Phys. A* **220**, 166 (1974).
- [29] D. Gerke, D. Tilley, N. Fletcher, and R. Williamson, *Nucl. Phys.* **75**, 609 (1966).
- [30] K. Gmür and H. H. Müller, *Helv. Phys. Acta* **46**, 807 (1973).
- [31] T. Gudehus, M. Cosack, R. Felst, and H. Wahl, *Nucl. Phys.* **80**, 577 (1966).
- [32] P. E. Hodgson and D. Wilmore, *Proc. Phys. Soc.* **90**, 361 (1967).
- [33] R. J. Jaszczak, R. L. Macklin, and J. H. Gibbons, *Phys. Rev.* **181**, 1428 (1969).
- [34] J. Jeronimo, G. Mani, F. Picard, and A. Sadeghi, *Nucl. Phys.* **43**, 417 (1963).
- [35] T. Katman, N. Fletcher, D. Tilley, and R. Williamson, *Nucl. Phys.* **80**, 449 (1966).
- [36] M. Kokkoris, P. Misailides, S. Kossionides, A. Lagoyannis, C. Zarkadas, R. Vlastou, C. Papadopoulos, and A. Kontos, *Nucl. Instrum. Methods Phys. Res., Sect. B* **249**, 81 (2006).
- [37] M. Kokkoris, P. Misaelides, A. Kontos, A. Lagoyannis, S. Harissopoulos, R. Vlastou, and C. Papadopoulos, *Nucl. Instrum. Methods Phys. Res., Sect. B* **254**, 10 (2007).
- [38] M. Kokkoris, P. Misaelides, S. Kossionides, C. Zarkadas, A. Lagoyannis, R. Vlastou, C. Papadopoulos, and A. Kontos, *Nucl. Instrum. Methods Phys. Res., Sect. B* **249**, 77 (2006).
- [39] M. T. McEllistrem, *Phys. Rev.* **111**, 596 (1958).
- [40] M. T. McEllistrem, K. W. Jones, R. Chiba, R. A. Douglas, D. F. Herring, and E. A. Silverstein, *Phys. Rev.* **104**, 1008 (1956).
- [41] J. P. de Carvalho and A. Reis, *Nucl. Instrum. Methods Phys. Res., Sect. B* **266**, 2263 (2008).
- [42] F. Papillon and P. Walter, *Nucl. Instrum. Methods Phys. Res., Sect. B* **132**, 468 (1997).
- [43] R. Poore, P. Shearin, D. Tilley, and R. Williamson, *Nucl. Phys. A* **92**, 97 (1967).
- [44] S. Tryti, T. Holtebekk, and J. Rekstad, *Nucl. Phys. A* **201**, 135 (1973).
- [45] S. Tryti, T. Holtebekk, and F. Ugletveit, *Nucl. Phys. A* **251**, 206 (1975).
- [46] Q. Liu, M. Febraro, R. J. deBoer, A. Boeltzig, Y. Chen, C. Cerjan, M. Couder, B. Frentz, J. Görres, E. A. Henry, E. Lamere, K. T. Macon, K. V. Manukyan, L. Morales, P. D. O'Malley, S. D. Pain, W. A. Peters, D. Schneider, C. Seymour, G. Seymour, E. Temanson, R. Toomey, B. Vande Kolk, J. Weaver, and M. Wiescher, *Phys. Rev. C* **100**, 034601 (2019).
- [47] F. Becchetti, R. Raymond, R. Torres-Isea, A. D. Fulvio, S. Clarke, S. Pozzi, and M. Febraro, *Nucl. Instrum. Methods Phys. Res., Sect. A* **820**, 112 (2016).
- [48] H. Prask, J. Rowe, J. Rush, and L. Schroder, *J. Res. Natl. Inst. Stand. Technol.* **98**, 1 (1993).
- [49] G. P. Lamaze, H. Chen-Mayer, J. K. Langland, and R. G. Downing, *Surf. Interface Anal.* **25**, 217 (1997).
- [50] R. Williams, J. Rowe, and P. Kopetka, The International Workshop on Cold Moderators for Pulsed Neutron Sources, Argonne National Laboratory, 1997 (unpublished).
- [51] W. M. Toney and A. W. Waltner, *Nucl. Phys.* **80**, 237 (1966).
- [52] J. F. Ziegler, M. D. Ziegler, and J. P. Biersack, *Nucl. Instrum. Methods Phys. Res. B* **268**, 1818 (2010).
- [53] See Supplemental Material at <http://link.aps.org/supplemental/10.1103/PhysRevC.101.025808> for AZURE2 input file and NIST report of target profile following beam bombardment.
- [54] B. Pehlivanovic, S. Avdic, P. Marinkovic, S. Pozzi, and M. Flaska, *Radiat. Meas.* **49**, 109 (2013).
- [55] M. Reginatto, *Radiat. Meas.* **45**, 1323 (2010).
- [56] J. Tain and D. Cano-Ott, *Nucl. Instrum. Methods Phys. Res., Sect. A* **571**, 728 (2007).
- [57] T. Goorley *et al.*, *Nucl. Technol.* **180**, 298 (2012).
- [58] S. A. Pozzi, E. Padovani, and M. Marseguerra, *Nucl. Instrum. Methods Phys. Res., Sect. A* **513**, 550 (2003).
- [59] M. Febraro, R. Toomey, S. D. Pain, K. A. Chipps, B. Becker, R. J. Newby, Z. Meisel, T. N. Massey, C. R. Brune, Q. Liu, R. J. deBoer, K. T. Macon, A. Boeltzig, J. O'Neill, M. S. Smith, M. Wiescher, D. Soltesz, I. Sultana, K. Brandenburg, S. Subendi, S. Paneru, T. Danely, and Y. Alberty-Jones, *Nucl. Instrum. Methods Phys. Res. A* **946**, 162668 (2019).
- [60] T. N. Massey, S. Al-Quraishi, C. E. Brient, J. F. Guillemette, S. M. Grimes, D. Jacobs, J. E. O'Donnell, J. Oldendick, and R. Wheeler, *Nucl. Sci. Eng.* **129**, 175 (1998).
- [61] T. N. Massey, D. K. Jacobs, S. I. Al-Quraishi, S. M. Grimes, C. E. Brient, W. B. Howard, and J. C. Yanch, *J. Nucl. Sci. Technol.* **39**, 677 (2002).
- [62] A. Antilla, J. Keinonen, M. Hautala, and I. Forsblom, *Nucl. Instrum. Methods* **147**, 501 (1977).
- [63] E. K. Warburton, D. E. Alburger, and D. J. Millener, *Phys. Rev. C* **22**, 2330 (1980).

- [64] A. M. Lane and R. G. Thomas, *Rev. Mod. Phys.* **30**, 257 (1958).
- [65] P. Descouvemont and D. Baye, *Rep. Prog. Phys.* **73**, 036301 (2010).
- [66] R. E. Azuma, E. Uberseder, E. C. Simpson, C. R. Brune, H. Costantini, R. J. de Boer, J. Görres, M. Heil, P. J. LeBlanc, C. Ugalde, and M. Wiescher, *Phys. Rev. C* **81**, 045805 (2010).
- [67] E. Uberseder and R. J. deBoer, AZURE2 User Manual, 2015.
- [68] C. R. Brune, *Phys. Rev. C* **66**, 044611 (2002).
- [69] M. Wang, G. Audi, A. H. Wapstra, F. G. Kondev, M. MacCormick, X. Xu, and B. Pfeiffer, *Chin. Phys. C* **36**, 1603 (2012).
- [70] W. Huang, G. Audi, M. Wang, F. Kondev, S. Naimi, and X. Xu, *Chin. Phys. C* **41**, 030002 (2017).
- [71] M. Wang, G. Audi, F. Kondev, W. Huang, S. Naimi, and X. Xu, *Chin. Phys. C* **41**, 030003 (2017).
- [72] F. Ajzenberg-Selove, *Nucl. Phys. A* **523**, 1 (1991).
- [73] F. Ajzenberg-Selove, *Nucl. Phys. A* **490**, 1 (1988).
- [74] K. Ikeda, T. Marumori, R. Tamagaki, and H. Tanaka, *Prog. Theor. Phys. Suppl.* **52**, 1 (1972).
- [75] J. Okołowicz, W. Nazarewicz, and M. Płoszajczak, *Fortschr. Phys.* **61**, 66 (2013).
- [76] F. Ajzenberg-Selove, *Nucl. Phys. A* **152**, 1 (1970).
- [77] N. F. Mangelson, B. G. Harvey, and N. K. Glendenning, *Nucl. Phys. A* **117**, 161 (1968).
- [78] K. Meier-Ewert, K. Bethge, and K.-O. Pfeiffer, *Nucl. Phys. A* **110**, 142 (1968).
- [79] J. L. Snelgrove and E. Kashy, *Phys. Rev.* **187**, 1259 (1969).
- [80] H.T. Fortune (private communication).
- [81] M. J. Harris, W. A. Fowler, G. R. Caughlan, and B. A. Zimmerman, *Annu. Rev. Astron. Astrophys.* **21**, 165 (1983).
- [82] G. R. Caughlan and W. A. Fowler, *At. Data Nucl. Data Tables* **40**, 283 (1988).
- [83] N. A. Roughton, T. P. Intrator, R. J. Peterson, C. S. Zaidins, and C. J. Hansen, *At. Data Nucl. Data Tables* **28**, 341 (1983).
- [84] D. Robertson, M. Couder, U. Greife, F. Strieder, and M. Wiescher, *Eur. J. Phys. Web Conf.* **109**, 09002 (2016).